Tập 15, số 3, tháng 9, 2026
https://doi.org/10.58334/vrtc.jtst.vol.15.934

Effect of Graphene Functionalization on the Microwave Absorption Performance of $Ni_{0.2}Zn_{0.8}Fe_2O_4$/graphene Nanoplatelet Composites

Ta Thu Trang[(1)]✉, Tran Quang Dat[(2)], Nguyen Nguyen Long[(2)], Do Dinh Trung[(1)], Dang Minh Thuy[(1)], Nguyen Van Vinh[(1)], Le Quoc Pham[(1)], Ha Minh Ngoc[(1)], Doan Quy Hieu[(1)], Dao Thanh Thuy[(1)], Tran Thi Toi[(3)]

[(1)] *Institute of Tropical Durability, Joint Vietnam-Russia Tropical Science and Technology Research Center, Hanoi, Vietnam*

[(2)] *Le Quy Don Technical University, Hanoi, Vietnam*

[(3)] *Military Science Academy, Hanoi, Vietnam*

✉ **Corresponding author**

E-mail: trang88py@gmail.com

ORCID: 0009-0000-7358-4009

How to cite this article

Ta, T. T., Tran, Q. D., Nguyen, N. L., Do, D. T., Dang, M. T., Nguyen, V. V., Le, Q. P., Ha, M. N., Doan, Q. H., Dao, T. T., & Tran, T. T. (2026). Effect of graphene functionalization on the microwave absorption performance of Ni0.2Zn0.8Fe2O4/graphene nanoplatelet composites. *Tạp chí Khoa học và Công nghệ Nhiệt đới*, 15(3), 81–95. https://doi.org/10.58334/vrtc.jtst.vol.015.934

Abstract

In this study, $Ni_{0.2}Zn_{0.8}Fe_2O_4$/graphene nanoplatelet (GNP) composites were prepared via a hydrothermal method for microwave absorption applications across the 2–18 GHz range. Graphene nanoplatelets (GNPs) were functionalized with hexamethylenediamine (HMDA) to modify their surface and facilitate the desponsition of ferrite nanoparticles . Structural and morphological analyses (XRD, SEM) confirmed the spinel ferrite formation and a superior distribution of nanoparticles on modified GNPs. Fourier transform infrared spectroscopy (FTIR) provided evidence for the surface functionalization of graphene through the appearance of characteristic aliphatic and nitrogen-containing bands. Raman spectra suggested surface modification of graphene and a closer morphological association between ferrite nanoparticles and graphene. Vibrating sample magnetometer (VSM) indicated soft magnetic behavior with optimized saturation magnetization. Crucially, frequency-dependent complex permittivity and complex permeability were investigated, showing that the HMDA-modified composites exhibit enhanced dielectric and magnetic loss tangents. Reflection loss (RL) analysis showed that the HMDA-modified graphene composite achieved a minimum RL of - 34 dB at 10 GHz with a thickness of 2.25 mm and a wide effective absorption bandwidth (EAB) of 4.24 GHz, outperforming the composite with unmodified graphene. The enhanced absorption performance is attributed to improved impedance matching and enhanced dielectric–magnetic loss mechanisms, which may be facilitated by the HMDA functionalization of graphene. These findings highlight the composite's potential as a radar-absorbing material.

Keywords: Composites; Graphene nanoplatelets; Microwave absorption; Radar absorbing materials; Spinel ferrite.

Introduction

In recent years, with the rapid development of electronic devices and radar technology, the issues of electromagnetic interference and radar detectability have attracted increasing attention. Therefore, the research and development of electromagnetic wave absorbing materials with high efficiency, low density, and good stability has become an important research direction in materials science. Radar absorbing materials can convert incident electromagnetic wave energy into thermal energy through dielectric and magnetic loss mechanisms, thereby reducing the intensity of the reflected waves (Houbi *et al*., 2021; Sugimoto, 2011; Chen *et al*., 2013; Lv *et al*., 2015; Naito & Suetake, 1971; Green & Chen, 2019).

Among various electromagnetic wave absorbing materials, spinel ferrites such as Ni–Zn ferrite have been widely studied due to their advantages including high chemical stability, suitable magnetic permeability, good magnetic loss, and tunable electromagnetic properties through compositional modification (Goldman, 2006; Amiri *et al*., 2011). However, single-phase ferrite materials often exhibit relatively low dielectric constants and limited impedance matching, which restrict their electromagnetic wave absorption performance (Meng *et al*., 2018). To overcome these limitations, combining ferrites with conductive nanomaterials, particularly graphene, has been demonstrated to be an effective strategy (Chen *et al*., 2013). GNPs possess a large specific surface area, high electrical conductivity, and

the ability to generate strong interfacial polarization, which can enhance dielectric loss and improve impedance matching in composite materials (Meng *et al*., 2018). However, pristine graphene tends to agglomerate due to strong π–π interactions between graphene layers and usually contains few active functional groups on its surface, which limits its dispersion and interaction with ferrite nanoparticles (Krishnamoorthy *et al*., 2013). One effective approach to improve this interaction involves the surface functionalization of graphene with various amine-containing compounds. This process introduces amino functional groups onto the graphene sheets, which enhances the affinity for metal ions during synthesis. Consequently, this promotes controlled nucleation and ensures a uniform distribution of ferrite nanoparticles across the graphene surface (Chen *et al*., 2024; Dreyer *et al*., 2010; Marcano *et al*., 2010). To date, significant breakthroughs in graphene/ferrite architectures have been achieved by introducing complex multi-component heterostructures or magnetic coupling mechanisms to enhance absorption efficiency. For instance, Chen *et al*. (2024) synthesized a complex Graphene/Fe_3C/$CoFe_2$/$CoFe_2O_4$ composite, utilizing exchange coupling between hard and soft magnetic phases to achieve a minimum reflection loss (RL_{min}) of -48.8 dB and an absorption bandwidth of 4.04 GHz at a thickness of 1.85 mm. Similarly, Tran *et al*. (2024) developed a core-shell structured $SrFe_{12}O_{19}$@Fe_3O_4@rGO composite via a multi-step hydrothermal method, which reached an outstanding (RL_{min}) of -62.3 dB and a broad bandwidth of 9.3 GHz at 2 mm thickness owing to its high surface area and enhanced multi-phase magnetic-dielectric losses. Furthermore, Dat *et al.* (2017) prepared a ternary rGO-$Cu_{0.5}Ni_{0.5}Fe_2O_4$-polyaniline nanocomposite exhibiting superparamagnetic behavior, which achieved a maximum RL of -40.7 dB at 9.8 GHz with an optimum matching thickness of 3 mm.

In this work, we focus on evaluating the strategic substitution of pristine graphene with hexamethylenediamine (HMDA)-functionalized graphene nanoplatelets to optimize the microwave absorption properties of $Ni_{0.2}Zn_{0.8}Fe_2O_4$/GNP composites. The impact of this substitution on structure, defects, and magnetic behavior was systematically analyzed using XRD, SEM, Raman, and VSM. Evaluation of electromagnetic parameters across the 2–18 GHz range demonstrates that interfacial modification is the key factor in enhancing electromagnetic loss and achieving high-performance reflection loss.

Materials and Methods

Materials

Nickel(II) nitrate hexahydrate ($Ni(NO_3)_2.6H_2O$), zinc nitrate hexahydrate ($Zn(NO_3)_2.6H_2O$), iron(III) nitrate nonahydrate ($Fe(NO_3)_3.9H_2O$), and sodium hydroxide (NaOH), all with a purity of ≥ 98%, were purchased from Merck (Germany) and used as received. The metal nitrates served as precursors for the synthesis of $Ni_{0.2}Zn_{0.8}Fe_2O_4$ spinel ferrite, while NaOH was used as the precipitating agent.

Graphene nanoplatelets were used as the conductive component to improve the dielectric properties of the composite materials. Graphene nanoplatelets were modified using hexamethylenediamine (HMDA) and N,N-dimethylformamide (DMF), with purities of ≥ 98% and ≥ 99.8%, respectively, both supplied by Merck (Germany), to improve the compatibility between graphene and ferrite nanoparticles.

All chemicals were of analytical grade and were used as received without further purification.

Methods

The equipment used in the synthesis process included a hydrothermal reactor and a laboratory drying oven. The hydrothermal reactor consisted of two parts: a sample container and an outer protective vessel. The inner container was made of polyphenylene (PPL) material, which is chemically inert, exhibits good thermal conductivity, and can withstand temperatures up to approximately 280 °C and pressures up to about 3 MPa. In addition, a laboratory drying oven (UNB400, Memmert, Germany) was used during sample processing.

The oven has a maximum operating temperature of 220 °C, a chamber volume of 53 L, and a temperature accuracy of 0.5 °C.

Functionalization of graphene nanoplatelets with HMDA

GNPs were functionalized with HMDA to improve their dispersion and facilitate the subsequent deposition of ferrite nanoparticles on the graphene surface. In a typical experiment, 1 g of graphene was dispersed in 60 mL of DMF using ultrasonic treatment to obtain a homogeneous suspension. Subsequently, 10 g of HMDA was added and the mixture was heated at 80°C under a nitrogen atmosphere with continuous stirring for 4 h (Bontaș *et al*., 2022).

After the reaction, the product was separated by vacuum filtration, washed several times with distilled water, methanol, and acetone, and then dried to obtain HMDA-functionalized graphene nanoplatelets (G-HMDA). The introduction of amine groups on the graphene surface improves its dispersion and promotes stronger interaction with ferrite nanoparticles in the composite material (Meng *et al*., 2018; Krishnamoorthy *et al*., 2013; Chen *et al*., 2024; Dreyer *et al*., 2010). Surface functionalization of graphene with amine-containing molecules has been widely reported to enhance interfacial compatibility and facilitate the uniform nucleation and growth of metal oxide nanoparticles on graphene sheets (Lv *et al*., 2015).

Hydrothermal synthesis of $Ni_{0.2}Zn_{0.8}Fe_2O_4$ with 2 wt% graphene nanoplatelet composites

The $Ni_{0.2}Zn_{0.8}Fe_2O_4$ (NZF)/graphene composites were synthesized via a hydrothermal method, utilizing both unmodified graphene nanoplatelets (G) and functionalized graphene nanoplatelets (FG). (Figure 1)

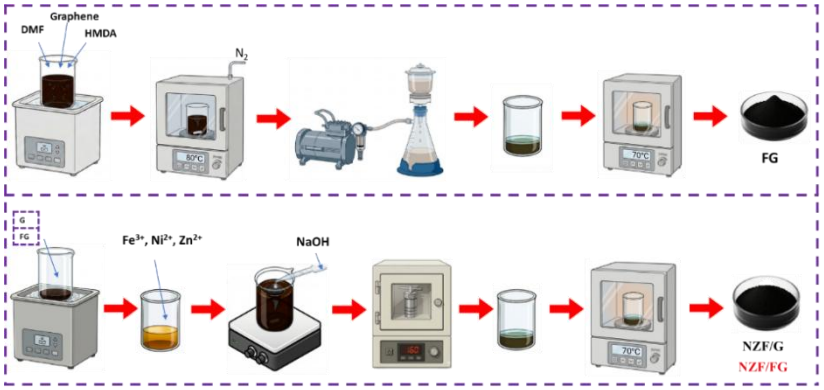

Figure 1. Fabrication diagram for the NZF/G and NZF/FG composites

In a typical process, 2 wt% of the respective graphene (relative to the final ferrite mass) was dispersed in distilled water using ultrasonication for 30 min to achieve a stable suspension. Simultaneously, stoichiometric amounts of $Ni(NO_3)_2.6H_2O$, $Zn(NO_3)_2.6H_2O$, and $Fe(NO_3)_3.9H_2O$ were dissolved in distilled water, with the final concentration of each precursor ion (Ni^{2+}, Zn^{2+}, and Fe^{3+}) carefully adjusted to exactly 0.1 M. The graphene suspension was then introduced into the precursor solution under vigorous stirring. Subsequently, a 2 M NaOH solution was added dropwise to adjust the pH to 10–12. The final blended mixture, with a total solution volume maintained at 120 mL, was subjected to constant magnetic stirring at 500 rpm and heated at 70°C for 30 min to ensure homogeneous ion adsorption onto the carbon templates. The mixture was transferred into a 200 mL Teflon-lined autoclave and subjected to hydrothermal treatment at 160°C for 6 h. After the reaction, the product was washed several times with distilled water and ethanol until the supernatant reached a neutral pH, and then dried at 100°C for 12 h to obtain $Ni_{0.2}Zn_{0.8}Fe_2O_4$/graphene nanoplatelet composite powder. The composite containing unmodified graphene is denoted as NZF/G, while the composite featuring functionalized graphene is designated as NZF/FG.

Characterization techniques

The crystal structure and phase composition of the ferrite-based composites were investigated

by X-ray diffraction (XRD) using a D2 Phaser diffractometer (Bruker, Germany). Diffraction patterns were recorded over the 2θ range of 15–80° with a scanning step of 0.02° and a slow scanning rate to ensure high signal resolution.

The surface morphology and microstructural characteristics of the synthesized materials were examined using field-emission scanning electron microscopy (FE-SEM, HITACHI S-4800). Prior to observation, the powder samples were dispersed onto conductive carbon tape and coated with a thin Au layer to improve surface conductivity and minimize charging effects during measurement. SEM micrographs acquired at different magnifications were used to evaluate particle morphology, particle size distribution, and the dispersion behavior of ferrite nanoparticles on graphene surfaces. Elemental composition and elemental distribution within the hybrid composites were analyzed using energy-dispersive X-ray spectroscopy (EDS) integrated with the SEM system. EDS spectroscopy was used to determine the elemental composition of the composites, whereas EDS elemental mapping was employed to visualize the spatial distribution of Ni, Zn, Fe, O, and C and to assess the compositional homogeneity of the synthesized materials. The chemical structures and surface functional groups of the pristine graphene and HMDA-functionalized graphene were investigated using Fourier-transform infrared spectroscopy (FTIR, Perkin spectrum two). The lattice vibrational modes were investigated via Raman spectroscopy using a Renishaw InVia Raman system equipped with a 633 nm laser (15 mW). Magnetic properties of the ferrite nanoparticles and hybrid composites were characterized using a vibrating sample magnetometer (VSM, MicroSense 3474-140) at room temperature under an applied magnetic field of up to 20 kOe. The magnetic hysteresis loops were used to determine key magnetic parameters, including saturation magnetization, remanent magnetization, and coercivity.

Electromagnetic properties were evaluated using a Keysight PNA-X N5242A vector network analyzer (VNA). Measurement specimens were prepared by blending the composite powders with a paraffin wax matrix at a 30:70 wt% ratio, then molded into toroidal shapes (inner diameter: 3.04 mm; outer diameter: 7.00 mm). To minimize experimental and geometric errors arising from the physical thickness measurement of the coaxial sample, the core thickness parameter in the Nicolson–Ross–Weir (NRW) extraction algorithm was finely calibrated (Dat *et al*., 2025). Specifically, the complex permittivity (ε_r) and complex permeability (μ_r) were iteratively calculated by sweeping the effective experimental thickness from 1.00 to 4.50 mm (with a 0.25 mm increment) to determine the mathematically optimized physical thickness for data extraction. The final frequency-dependent ε_r and μ_r values used for the composite were obtained by averaging these thickness-dependent datasets. Building upon transmission line theory, a comprehensive suite of microwave absorption indicators-including reflection loss (RL), dielectric and magnetic loss tangents, eddy current coefficients, and Cole–Cole plots-was evaluated to characterize the material's electromagnetic attenuation performance.

Results

Morphological, structural and magnetic data

The surface morphologies of the NZF/G and NZF/FG samples are presented in Figure 2(a, b). NZF/G exhibits local ferrite agglomeration and severe graphene restacking (multi-layered regions). NZF/FG displays localized ferrite clusters resting on highly exfoliated, non-restacked graphene sheets. The elemental compositions of the composites were determined using Energy-Dispersive X-ray spectroscopy (EDS), as shown in Figure 2(c, d). As shown in Figure 2(c, d), the characteristic peaks of C, O, Fe, Ni, and Zn are verified. Upon functionalization, the C-content increases sharply from 20.75 wt.% to 28.28 wt.%, while the metallic elements (Fe, Ni, Zn) show a relative decrease.

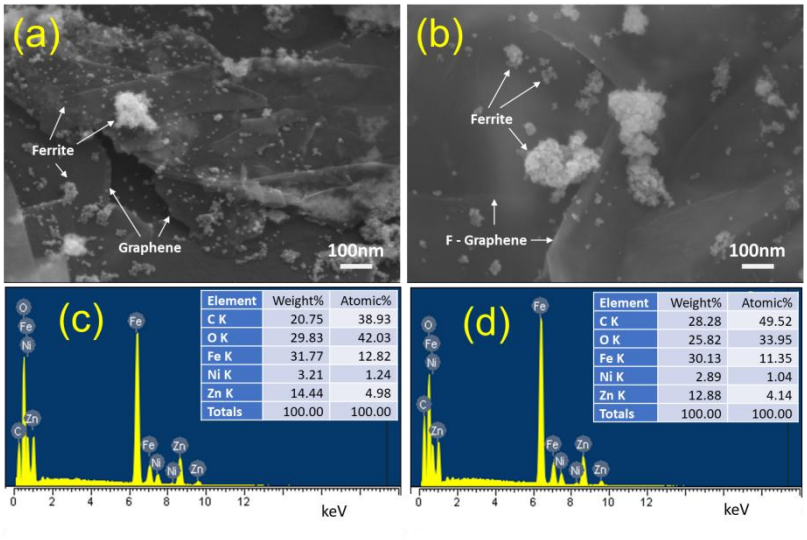

Figure 2. SEM images of (a) NZF/G and (b) NZF/FG, EDS spectra of (c) NZF/G and (d) NZF/FG

The EDS elemental mapping results for the NZF/G and NZF/FG composites are shown in Figure 3 (a, b). The maps confirm the presence of C, O, Fe, Ni, and Zn in both samples. Fe, Ni, Zn, and O are distributed across the graphene matrix together with the carbon signal, indicating the coexistence of the ferrite and graphene phases. Compared with the NZF/G sample, the NZF/FG composite exhibits a more uniform distribution of the ferrite-related elements over the graphene sheets.

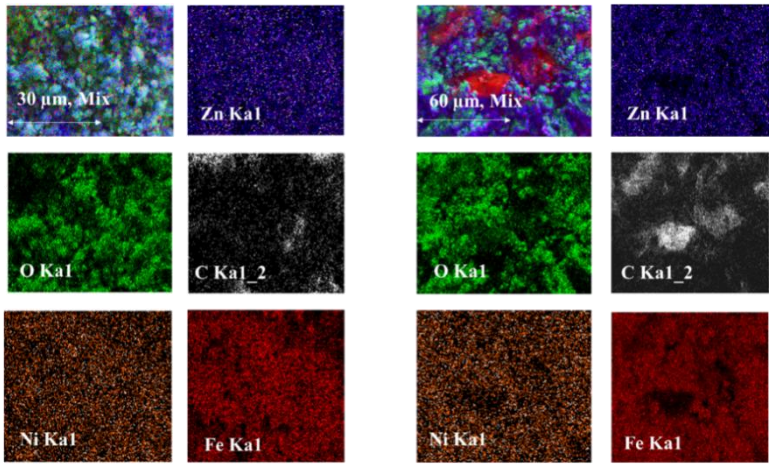

Figure 3. EDS elemental mapping of (a) NZF/FG and (b) NZF/G composites

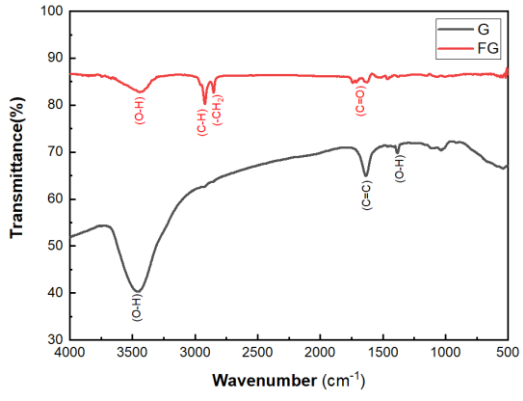

Figure 4. FTIR spectra of G and FG

The FTIR spectra of pristine graphene and HMDA-functionalized graphene are comparatively presented in Figure 4. For the pristine graphene, the spectrum exhibits a broad and prominent absorption band centered at 3455 cm^{-1}, accompanied by a sharp peak at 1635 cm^{-1} and a weak band at 1384 cm^{-1}. In contrast, the spectrum of the HMDA-functionalized graphene demonstrates substantial modifications. The broad band around 3455 cm^{-1} shifts slightly to 3443 cm^{-1}. Notably, two newly emerged, highly intense, and sharp peaks are observed at 2921 and 2852 cm^{-1}.

Furthermore, two additional individual peaks are clearly resolved at 1741 and 1713 cm^{-1}. Figure 5(a, b) illustrates the D-band (~1350 cm^{-1}) and G-band (~1580 cm^{-1}) for all samples. The I_D/I_G intensity ratio drops noticeably for G-HMDA and NZF/FG compared to their unmodified counterparts. For NZF/FG, the active ferrite modes (E_g, T_{2g}, A_{1g}) appear at 351, 486, and 665 cm^{-1}, exhibiting a blue-shift from the 340, 471, and 660 cm^{-1} peaks seen in NZF/G.

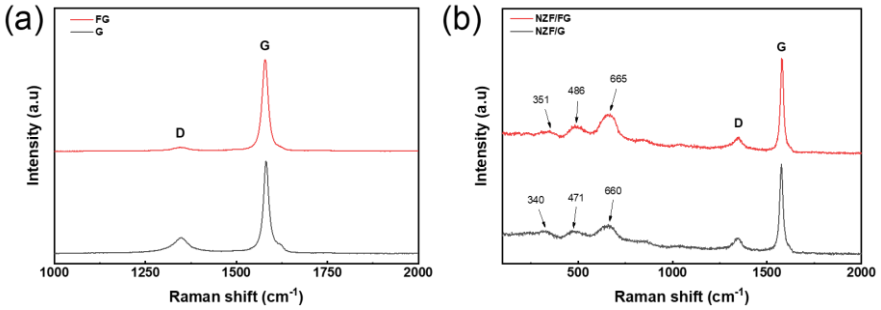

Figure 5. Raman spectra of the G, FG, NZF/G and NZF/FG

Figure 6 confirms the cubic spinel ferrite phase (JCPDS card no. 052-0279) for both composites with peaks at 18°, 30°, 35°, 43°, 53°, 57°, and 63°.

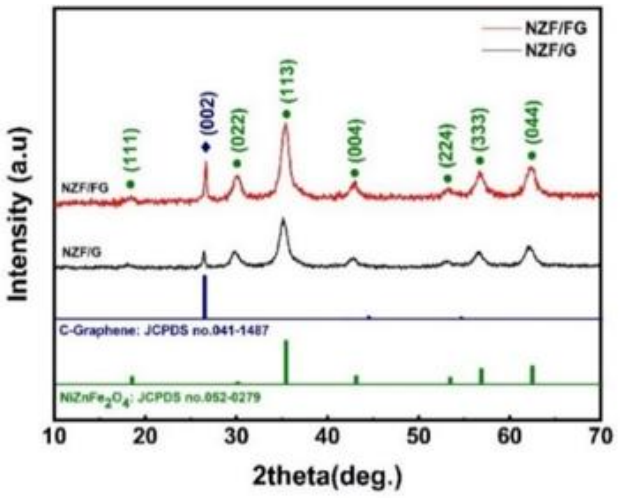

Figure 6. XRD patterns of NZF/G and NZF/FG

The average crystallite size was estimated using the Scherrer equation (Tran *et al.*, 2024):

$$D = \frac{K \times \lambda}{\beta \times cos\theta} \quad (1)$$

where D (nm) is the crystallite size, K = 0.89 with shape factor for near-spherical crystals), λ = 0.15406 nm is the X-ray wavelength, β is the full width at half maximum of the diffraction peak, corrected for instrumental broadening, θ is the Bragg angle. To ensure scientific rigor and eliminate qualitative ambiguity, the β values were extracted via a rigorous mathematical peak-fitting method on the core (311) reflection, and the corresponding calculation errors were propagated systematically. The refined calculations demonstrate that the crystallite size remains highly consistent across both samples, yielding approximately 8.3 ± 0.4 nm for NZF/G and 8.2 ± 0.4 nm for NZF/FG. Because the calculated FWHM values (1.01° and 1.02°) and the broad profile lines shapes are virtually identical within their experimental error margins, the previous subjective statement claiming that the NZF/FG sample possessed sharper or more intense peaks has been omitted. This highly confined grain size in the range of 8.2–8.3 nm confirms the nanocrystalline nature of the spinel ferrite phase embedded within the carbon matrix.

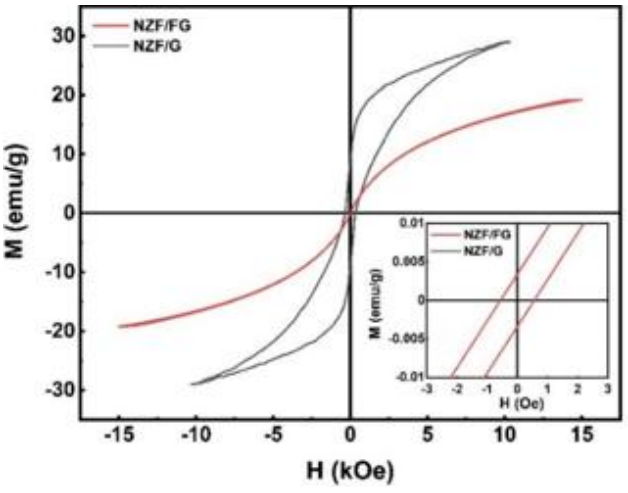

Figure 7. Hysteresis loops of NZF/G and NZF/FG at room temperature

Figure 7 displays the soft magnetic hysteresis loops. The NZF/G sample exhibited typical

ferromagnetic characteristics with a saturation magnetization (M_s) of 28 emu/g, a remanent magnetization (M_r) of 9 emu/g, and a coercive field (H_c) of 340 Oe. In contrast, for the functionalized NZF/FG composite, the M_s value noticeably decreased to 17 emu/g. This reduction in saturation magnetization is expected and directly attributed to the incorporation of the non-magnetic G-HMDA phase, which lowers the overall mass magnetic density of the composite material. Furthermore, the NZF/FG sample demonstrated a near-zero remanence (M_r ~ 0 emu/g) and an extremely low coercivity (H_c = 0.5 Oe).

Electromagnetic and microwave absorption data

The potential of the synthesized composites for practical microwave absorption was assessed through theoretical simulations based on transmission line theory. Utilizing the experimentally measured complex permittivity and complex permeability, the reflection loss was calculated using the following expressions (Dat *et al*., 2017):

$$Z_{in} = Z_0\sqrt{\frac{\mu_r}{\varepsilon_r}}\tanh\left(j\frac{2\pi ft}{c}\sqrt{\mu_r\varepsilon_r}\right) \quad (2)$$

$$RL\ (dB) = -20\ log\left|\frac{Z_{in}-Z_0}{Z_{in}+Z_0}\right| \quad (3)$$

where Z_{in} denotes the input impedance of the composite material, Z_0 represents the characteristic impedance of free space, f is the frequency of the microwave frequency, t is the thickness of the absorber, and c is the speed of light in vacuum.

Figure 8 illustrates the frequency-dependent reflection loss curves for the NZF/G and NZF/FG composites at various matching thicknesses. In terms of absorption depth, the NZF/FG composite (Fig. 8(b)) exhibits a significantly enhanced performance compared to its unmodified counterpart (Fig. 8(a)). Specifically, at an optimal matching thickness of 2.25 mm, the functionalized sample achieves a minimum reflection loss (RL_{min}) of approximately -34 dB at a frequency of 10 GHz. In contrast, the pristine graphene composite (NZF/G) only reaches an RL_{min} of –30 dB within the same frequency region.

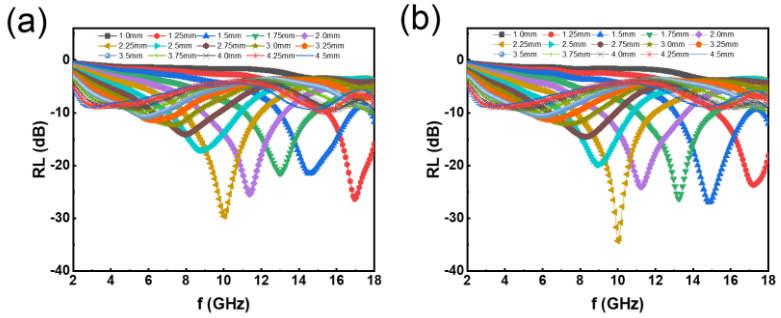

Figure 8. RL curves as a function of frequency and thickness ranges of 2–18 GHz and 1.0-4.5 mm of (a) NZF/G and (b) NZF/FG

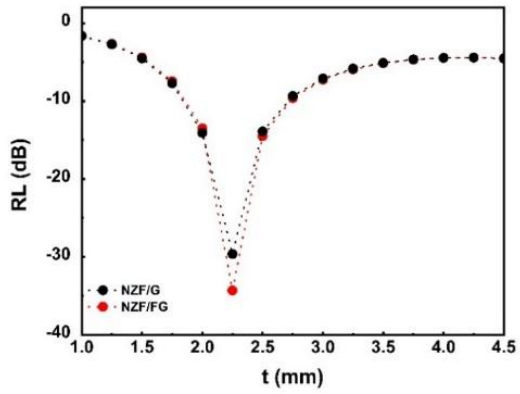

Figure 9. RL values for 1.0-4.5 mm thickness of NZF/G and NZF/FG at 10 GHz

Figure 9 highlights the resonant peak at 2.25 mm for both samples at 10 GHz. The effective absorption bandwidth (EAB), defined as the frequency range where RL ≤ -10 dB (representing 90% microwave absorption), is a critical metric for evaluating the practical versatility of an electromagnetic absorber.

Figure 10 compares the EAB values for the NZF/G and NZF/FG composites across a thickness range of 1.25–3.5 mm. Both composites demonstrate a clear frequency-tuning characteristic: as the thickness increases, the EAB regions systematically shift from the

high-frequency Ku-band (12-18 GHz) toward the lower X-band (8-12 GHz) and C-band (6-8 GHz). This trend is consistent with the quarter-wavelength matching mechanism, indicating that the absorption band can be precisely adjusted to meet different radar stealth requirements by simply controlling the coating thickness. At a thickness of 2.25 mm, the NZF/G composite exhibits an EAB of 3.92 GHz (ranging from 8.0 to 11.92 GHz), failing to fully encompass the critical X-band. In stark contrast, the functionalized NZF/FG composite achieves an expanded EAB of 4.24 GHz, spanning from 7.76 to 12.0 GHz. Remarkably, this allows the NZF/FG sample to achieve full coverage of the X-band at a single thickness of 2.25 mm, a feat not attained by the unmodified counterpart.

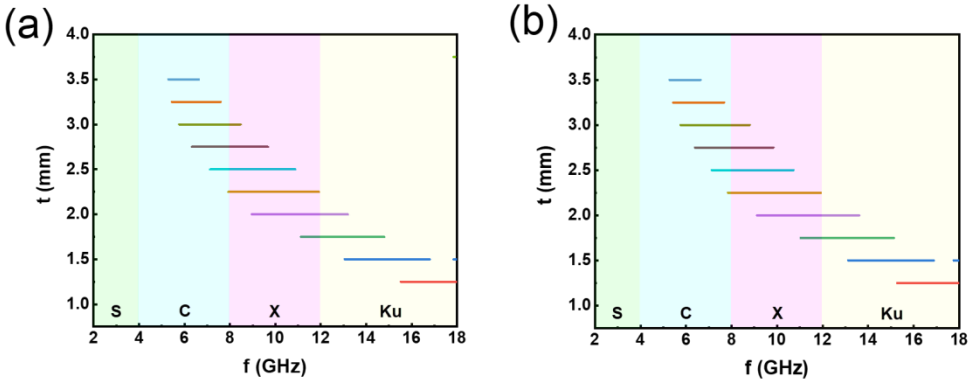

Figure 10. EAB values for the thickness range of 1.25-3.5 mm of (a) NZF/G and (b) NZF/FG

Figures 11(a, b) display the real part (ε') and imaginary part (ε'') of the relative complex permittivity, where NZF/FG exhibits higher ε' and ε'' values than NZF/G. Conversely, Figure 11(c, d) reveals that NZF/G maintains a higher real permeability (μ'), while NZF/FG possesses a significantly higher imaginary permeability (μ'').

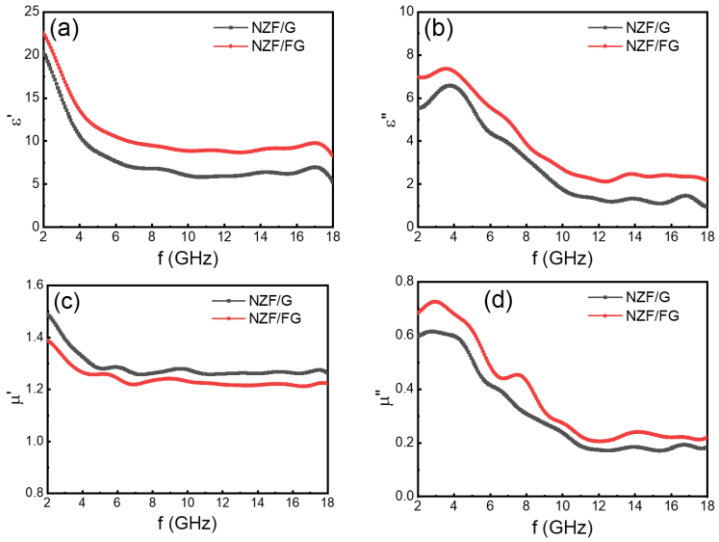

Figure 11. Frequency dependence of (a, b) relative complex permittivity and (c, d) relative complex permeability of NZF/G and NZF/FG

Discussion

Structural, morphological, and spectroscopic characterization

The morphological and structural data from SEM, EDS, EDS elemental mapping, Raman, and XRD indicate that the modification process using HMDA primarily alters the dispersion state of the graphene matrix-transitioning it from a restacked, multi-layered framework to an open, well-exfoliated configuration-rather than merely changing the uniform distribution of the ferrite nanoparticles (Tran *et al.*, 2024). The marked

increase in carbon concentration observed by EDS analysis, is consistent with the surface functionalization of graphene by HMDA, which introduces additional hydrocarbon (-CH_2-) chains and amine (-NH_2-) groups onto the graphene surface. Consistent with these observations, the EDS elemental mapping images demonstrate a more homogeneous spatial distribution of the ferrite-related elements (Fe, Ni, Zn, and O) over the graphene framework in the NZF/FG composite compared with the NZF/G sample. This finding suggests that the improved dispersion of HMDA-functionalized graphene provides a more accessible surface for the deposition of ferrite nanoparticles. Concurrently, the relative drop in the weight percentages of Fe, Ni, and Zn does not indicate a loss or degradation of the ferrite phase, but rather represents a surface dilution effect resulting from the increased mass fraction of the organic modifier coating the graphene support layers.

The FTIR spectra are consistent with the surface modification of graphene following HMDA treatment. In the pristine sample, the bands at 3455 and 1384 cm^{-1} are assigned to the stretching and in-plane bending modes of hydroxyl (-OH) groups from either surface-adsorbed moisture or residual oxygen defect species. The peak at 1635 cm^{-1} corresponds to the skeletal C=C stretching of the unfunctionalized sp^2-hybridized aromatic carbon network. The structural introduction of HMDA introduces profound spectral fingerprints. The appearance of the intense doublet at 2921 and 2852 cm^{-1} is unambiguously attributed to the asymmetric and symmetric stretching vibrations of aliphatic C-H bonds in the methylene (-CH_2-) repeat units. The emergence of these characteristic bands, which are absent in pristine graphene, is consistent with the introduction of HMDA-derived alkyl chains onto the graphene surface. Furthermore, the integration of nitrogen-containing moieties is confirmed by the shift of the broad hydroxyl band to 3443 cm^{-1}, which is caused by the strong overlap with the characteristic N-H stretching vibrations of primary or secondary amine groups. The broad absorption bands appearing at 1741 and 1713 cm^{-1} can be assigned to the residual oxygen-containing carbonyl functional groups on the graphene surface and the complex electrostatic or hydrogen-bonding interactions between the amine (-NH_2-) groups of the HMDA molecules and these oxygenated site (Dat *et al*., 2017).

In the Raman analysis (Figure 5), the noticeable decrease in the I_D/I_G ratio observed for the G-HMDA and NZF/FG samples should not be interpreted as a direct reduction in the intrinsic structural defects of the graphene lattice. Instead, this downward trend is primarily driven by the surface coverage effect and the significant suppression of the disordered π-π restacking and re-agglomeration of the graphene nanoplatelets, induced by the steric hindrance of the linear HMDA spacer molecules. The deposition of ferrite nanoparticles on the HMDA-functionalized graphene sheets may also influence the surface optical scattering properties and limits the localized fluorescence background contribution. Consequently, this modification helps preserve a higher relative degree of exposed in-plane sp^2 structural domains within the carbon network, which plays a key role in balancing the dielectric loss and adjusting the overall impedance matching profile of the composite (Krishnamoorthy *et al*., 2013). More importantly, the blue-shift observed in the active vibrational modes (E_g, T_{2g}, A_{1g}) of the spinel ferrite phase for the NZF/FG sample suggests a change in the local vibrational environment of the ferrite nanoparticles after HMDA treatment. However, the present Raman results do not directly establish the nature of the interfacial bonding between ferrite nanoparticles and graphene. The improved spatial distribution of ferrite nanoparticles on HMDA-functionalized graphene may facilitate more effective dielectric and magnetic interactions within the composite (Tran *et al*., 2024).

From a crystallographic standpoint, the constant average crystallite size indicates that the functionalization of graphene does not interfere with the crystal nucleation and growth kinetics of the ferrite phase. Under the hydrothermal conditions at 160 °C, the crystalline evolution is

entirely governed by core parameters such as temperature, reaction duration, and precursor concentration, while the graphene sheets simply serve as a supportive hosting substrate. The XRD patterns indicate that both samples possess comparable crystallite sizes and similar crystallinity. The well-exfoliated environment provided by G-HMDA prevents spatial cluttering, allowing for a highly uniform distribution and oriented growth of ferrite nanoparticles across the open framework.

Thus, current analysis of results supports the surface chemical functionalization of graphene by HMDA and the improved binding state between ferrite nanoparticles and graphene. However, we did not directly identify the chemical bonding between the two phases. Further studies using techniques such as XPS or HRTEM are needed to elucidate the bonding mechanism between the two phases.

Nature of the magnetic phase transition

The low values of remanence (M_r) and coercivity (H_c) observed in the *M–H* loops (Figure 7) indicate that both composites retain typical soft magnetic behavior, ensuring rapid magnetization and demagnetization responses under an alternating external magnetic field. However, their specific magnetization pathways differ significantly due to the structural changes induced by functionalization. The NZF/FG sample exhibits a slower approach to magnetic saturation and a drastic drop in M_r and H_c to near-zero values ($M_r \sim 0$ emu/g, $H_c = 0.5$ Oe), marking a clear transition toward a superparamagnetic-like behavior. According to the established magnetic theories, typical spinel ferrite nanoparticles exhibit a transition from a ferromagnetic to a superparamagnetic state when their grain size falls below the critical threshold of approximately 10 nm (Jiles, 2015). Since the crystal size of the ferrite phase in our synthesized NZF/FG composite is confined to approximately 8.2–8.3 nm (as calculated from the XRD peak-fitting analysis), the observed collapse of remanence and coercivity rests on a solid structural foundation. This shift is further governed by the spatial arrangement of its constituent phases. The introduction of HMDA significantly reduces the restacking of graphene sheets, which increases the effective surface area but leads to a discontinuous, isolated distribution of the magnetic phase. Consequently, the long-range magnetic exchange interactions between adjacent ferrite clusters are interrupted by these organic isolation barriers. Once the external field is removed, the magnetically isolated nanoparticles easily return to a random orientation via thermal activation. Conversely, the severe restacking in the NZF/G sample creates highly dense, multi-layered regions (Tran *et al*., 2024). This high particle connectivity preserves continuous inter-particle coupling and stabilizes the magnetic domains, making it harder for the spins to relax and resulting in both a rapid alignment toward saturation and larger retained M_r (9 emu/g) and H_c (340 Oe).

Additionally, as corrected from the raw experimental records, the M_s decreases from 28 emu/g for NZF/G to 17 emu/g for NZF/FG. This reduction stems primarily from the increased mass fraction of the non-magnetic phases (the carbon skeleton and -NH_2- functional groups) which exerts a dilution effect on the total magnetic moment. It is further influenced by nanoscale surface pinning effects, as well as spin canting or disorder at the grain boundaries of the isolated nanoparticles. For radar stealth applications, the transition toward superparamagnetic-like behavior in the functionalized sample is highly advantageous, as minimizing residual magnetization effectively eliminates parasitic reflections at the air-absorber interface.

Microwave absorption and electromagnetic loss mechanisms

The minimum reflection loss of –34 dB demonstrates that the functionalized NZF/FG composite can successfully dissipate over 99.96% of the incident microwave energy, markedly outperforming the unmodified version (Tho *et al*., 2024).

The RL spectra for both samples reveal a clear dependence of the absorption peaks on the

material thickness. As the thickness decreases, the RL_{min} peaks systematically shift toward the higher frequency region, specifically into the Ku-band (12–18 GHz). This phenomenon is in strict accordance with the quarter-wavelength ($\lambda/4$) matching model, where the peak frequency (f_m) and matching thickness (t_m) satisfy the relation (Tho *et al*., 2024):

$$t_m = n\lambda/4 = nc/(4f_m\sqrt{\varepsilon_r\mu_r}) \quad (4)$$

This mathematical relationship confirms that the operating absorption band is highly configurable rather than fixed. By systematically controlling the coating thickness, the resonance frequency can be precisely adjusted across different microwave bands. Consequently, this provides a practical approach to engineering customized absorber coatings that meet specific radar stealth requirement.

The significant expansion of EAB to 4.24 GHz-achieving complete coverage of the critical X-band at a single thickness of 2.25 mm-is a direct consequence of optimized impedance matching. In the raw NZF/G composite, the severe restacking of graphene sheets often leads to excessive localized electrical conductivity pathways. This creates a severe imbalance between the complex permittivity and permeability, causing the incoming microwave fronts to reflect off the front surface rather than entering the material bulk (Dat *et al*., 2017). For the NZF/FG composite, the well-exfoliated graphene flakes maintain a moderate and well-dispersed conductivity profile. This optimized state establishes a stable impedance matching condition, allowing electromagnetic waves to penetrate deeply into the material interior for internal attenuation (Tran *et al*., 2024).

The downward frequency dispersion seen in the complex permittivity curves (Figure 11(a, b)) is rooted in typical dielectric relaxation, where the high-frequency oscillation of the external electric field outpaces the response of the electric dipoles, preventing synchronous alignment. The superior ε' and ε'' values of the NZF/FG composite are driven by the grafted amino groups, which enrich the material's molecular dipole density and trigger the Maxwell-Wagner interfacial polarization effect (interfacial polarization at the ferrite–graphene boundaries). The nano-sized ferrite particles anchored onto the open graphene sheets form numerous micro-capacitor networks, generating robust energy dissipation driven by multi-interfacial polarization within the unique heterostructure (Nguyen *et al*., 2024).

For the complex permeability (Figure 11(c, d)), the superior real part of the NZF/G sample is tied to its restacked architecture, which preserves long-range magnetic exchange pathways. However, the significantly enhanced imaginary part in the NZF/FG sample demonstrates optimized magnetic energy dissipation channels. This elevated magnetic loss is fueled by natural ferromagnetic resonance and domain wall resonance within the Ni-Zn ferrite phase, acting in synergy with the improved dielectric loss components to yield superior total attenuation (Dat *et al*., 2025).

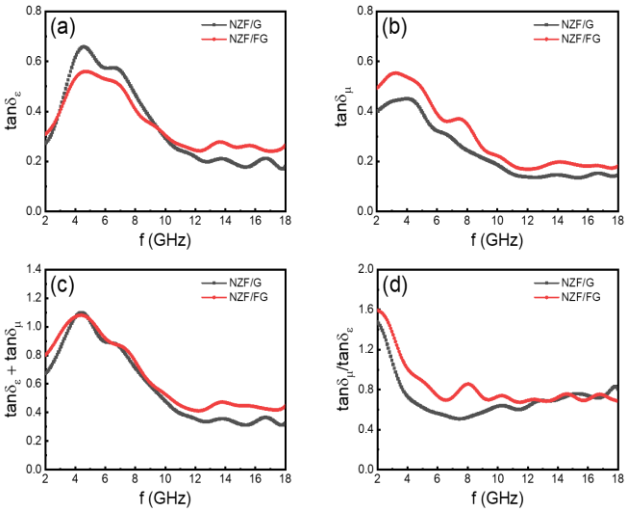

Figure 12. Frequency dependence of (a) dielectric loss tangent, (b) magnetic loss tangent, (c) total loss tangent, and (d) loss capacity matching of NZF/G and NZF/FG

Figures 12(a) and 12(b) display the dielectric loss tangent (tan $\delta_\varepsilon = \varepsilon''/\varepsilon'$) and magnetic loss tangent (tan $\delta_\mu = \mu''/\mu'$), respectively. The tan δ_ε values for both samples remain relatively high (ranging from 0.2 to 0.7), indicating that dielectric loss is a major contributor to microwave attenuation. While the unmodified NZF/G shows slightly higher peaks in some regions, the NZF/FG sample exhibits a more stable and sustained dielectric loss across the

10–18 GHz range. Notably, the NZF/FG composite (red curve) demonstrates a significantly higher tan $\delta_\mu = \mu''/\mu'$ throughout the 2–18 GHz spectrum compared to NZF/G. This confirms that HMDA functionalization enhances magnetic energy dissipation, despite the slight reduction in magnetic storage observed in the permeability data.

Figure 12(c) shows the total loss tangent (tan δ_μ + tan δ_ε), which represents the combined attenuation capability. The NZF/FG composite consistently outperforms the unmodified sample, particularly in the high-frequency range (12–18 GHz), suggesting a more powerful overall EM wave dissipation capacity. Furthermore, Figure 12(d) illustrates the loss capacity matching (tan δ_μ/tan δ_ε). For an ideal absorber, a balance between magnetic and dielectric losses is essential for optimal impedance matching. The NZF/FG sample maintains values closer to a balanced state compared to NZF/G, especially in the S, C and X bands, which explains its superior reflection loss performance.

To distinguish between polarization relaxation and conduction loss, the Cole–Cole plots were analyzed based on the Debye relaxation theory. According to the expression (Dat *et al*., 2025):

$$\left(\varepsilon' - \frac{\varepsilon_s + \varepsilon_\infty}{2}\right)^2 + (\varepsilon'')^2 = \left(\frac{\varepsilon_s - \varepsilon_\infty}{2}\right)^2 \quad (5)$$

where ε_s is the static permittivity and ε_∞ is the high-frequency permittivity limit.

As shown in Figure 13(a), both composites exhibit multiple overlapping semicircles, indicating the presence of multiple relaxation mechanisms. The plot for the functionalized sample shows significantly expanded and more pronounced semicircles compared to the NZF/G sample. This expansion confirms that HMDA-modification successfully maximizes interfacial polarization (Maxwell-Wagner effect) at the ferrite–graphene boundaries. The larger radius of these arcs reflects a higher energy storage-to-loss transition driven by the particle-on-sheet architecture (Dat *et al*., 2017).

To identify the specific contributions of magnetic loss-distinguishing between eddy current effects and natural resonance-the eddy current factor (C_0) was evaluated using the relation (Tran *et al*., 2026):

$$C_0 = \mu''(\mu')^{-2}f^{-1} \quad (6)$$

According to classical electromagnetic theory, if magnetic loss is solely governed by eddy currents, the C_0 value should remain constant across the frequency range. Conversely, if C_0 fluctuates, it indicates the presence of natural resonance or exchange resonance (Luu *et al*., 2026).

The frequency-dependent C_0 curves in Figure 13(b) reveal a two-stage evolution of magnetic loss mechanisms. In the low-frequency regime (2–10 GHz), the sharp decline in C_0 values confirms that natural ferromagnetic resonance is the primary dissipation driver. Conversely, the stabilization into a plateau from 10–18 GHz indicates that eddy current loss becomes the dominant mechanism in the high-frequency Ku-band. Notably, the NZF/FG composite consistently exhibits higher C_0 values than NZF/G, suggesting that the exfoliated, functionalized graphene matrix facilitates more efficient micro-current loops. By optimizing ferrite dispersion and strengthening the coupling between magnetic and conductive phases, HMDA-functionalization fundamentally enhances the material's magnetic attenuation capacity.

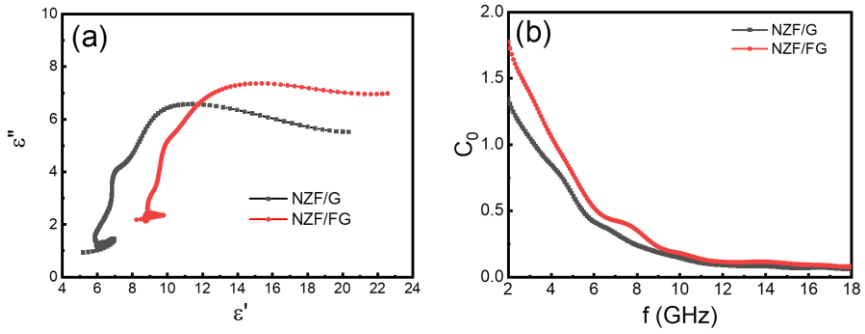

Figure 13. (a) Cole-Cole plots and (b) C_0 curves for NZF/G and NZF/FG

The enhanced efficacy of the NZF/FG system can be attributed to several critical factors induced by the HMDA modification. As suggested by the SEM and Raman results, HMDA treatment helps reduce the restacking of graphene nanopletelets, leading to a more open graphene framework with a larger accessible surface area. This structural transition facilitates a more efficient entry of microwaves into the material, thereby optimizing the impedance matching. Without functionalization, the high reflection at the air-absorber interface typically limits the amount of energy that can be internally dissipated (Dat *et al*., 2017). Furthermore, the blue shift of the ferrite Raman modes suggests a modified local vibrational environment after HMDA functionalization. Together with the more homogeneous distribution of ferrite nanoparticles on the graphene surface, this may contribute to enhanced interfacial polarization. The functional groups introduced by HMDA may facilitate Maxwell–Wagner–Sillars interfacial polarization at the ferrite/graphene interfaces. Together with the enhanced dielectric and magnetic loss characteristics, these effects are consistent with the higher attenuation constant observed for the NZF/FG composite (Luu *et al*., 2026). Consequently, the present results suggest that graphene functionalization with HMDA is an effective approach for improving the microwave absorption performance of ferrite/graphene composites (Nguyen *et al*., 2024).

To objectively evaluate the microwave absorption performance of the NZF/FG composite, a comparative analysis with related ferrite/graphene absorbers is presented in Table 1. The tabulated data indicate that although Cr-Co-Ni ferrite/GO (Dabla *et al*., 2025), Al-Cu ferrite/rGO (Singh *et al*., 2022), and Zn ferrite/rGO (Shu *et al*., 2018) possess deeper RL_{min} values, their application is limited by a narrower bandwidth. Conversely, absorbers with a wider bandwidth, such as Mg-Co ferrite/MGO (Zheng *et al*., 2025) and Co-Zr ferrite/rGO (Gunasekaran *et al*., 2021), suffer from either lower attenuation or an excessive matching thickness. In contrast, the optimized NZF/FG composite exhibits a superior balance of absorption properties, achieving a strong reflection loss and a broad EAB that completely covers the target frequency band at a significantly minimized matching thickness.

Table 1. Comparison of microwave absorption performance of NZF/FG composites with other related absorbers

Sample name	RL_{min} (dB)	EAB (GHz)	d (mm)	Ref.
Cr-Co-Ni ferrite/GO	-49.0	0.75	2.50	(Dabla et al., 2025)
Al-Cu ferrite/rGO	-35.7	3.55	2.20	(Singh et al., 2022)
Mg-Co ferrite/MGO	-29.0	5.19	2.00	(Zheng et al., 2025)
Co-Zr ferrite/rGO	-31.9	4.00	5.00	(Gunasekaran et al., 2021)
Zn ferrite/rGO	-41.0	3.20	2.50	(Shu et al., 2018)
NZF/FG	-34.0	4.24	2.25	This work

Conclusion

In summary, $Ni_{0.2}Zn_{0.8}Fe_2O_4$/graphene nanoplatelet composites were prepared through a hydrothermal process. Structural and morphological analyses indicate that the chemical functionalization of GNPs using hexamethylenediamine (HMDA) suppresses graphene restacking and promotes a more homogeneous distribution of spinel ferrite nanoparticles on the graphene sheets. While magnetic measurements classified the composites as soft magnetic materials with characteristic superparamagnetic-like behavior, the microwave absorption properties were significantly enhanced through this surface modification. Specifically, the NZF/FG composite achieved a remarkable minimum reflection loss of -34 dB at 10 GHz with a thickness of 2.25 mm, outperforming the unmodified sample and exhibiting EAB of 4.24 GHz that fully covers the entire X-band frequency range. This superior performance is primarily attributed to the

optimized impedance matching and the enhanced synergy between dielectric and magnetic loss mechanisms, positioning the NZF/FG composite as a highly promising candidate for potential radar-absorbing material.

Funding: *This research was funded by the Joint Vietnam–Russia Tropical Science and Technology Research Center under the project entitled "Investigation and Fabrication of Radar Wave Absorbing Coatings in the 8–12 GHz Frequency Band Based on Spinel Ferrite/Graphene Nanoplatelet Composite Materials" (Project No. ĐB.Đ2.01/25).*

Author contributions*: Author Contributions: Ta Thu Trang: Conceptualization, Methodology, Investigation, Data Curation, Formal Analysis, Writing – Original Draft. Tran Quang Dat: Investigation, Writing – Original Draft, Formal Analysis. Nguyen Nguyen Long: Formal Analysis. Tran Thi Toi: Formal Analysis. Do Dinh Trung: Investigation, Data Curation. Dang Minh Thuy: Conceptualization. Nguyen Van Vinh: Formal Analysis, Data Curation. Le Quoc Pham: Formal Analysis, Visualization, Validation. Ha Minh Ngoc: Investigation, Formal Analysis. Doan Quy Hieu: Investigation, Formal Analysis. Dao Thanh Thuy: Investigation, Formal Analysis. All authors have read and agreed to the published version of the manuscript.*

Data Availability Statement: *All relevant data supporting the findings of this study are included within the article and its supplementary materials.*

Statement on the use of Generative AI*: AI tools were used solely for language editing and not for generating scientific content. All data, analyses, and interpretations were performed and verified by the authors, who take full responsibility for the manuscript.*

Conflict of interest statement*: The authors declare that they have no known competing financial interests or personal relationships that could have influenced the work reported in this manuscript.*

References

Amiri, G. R., Yousefi, M. H., Abolhassani, M. R., Manouchehri, S., Keshavarz, M. H., & Fatahian, S. (2011). Magnetic properties and microwave absorption in Ni–Zn and Mn–Zn ferrite nanoparticles synthesized by low-temperature solid-state reaction. *Journal of Magnetism and Magnetic Materials, 323*(6), 730–734. https://doi.org/10.1016/j.jmmm.2010.10.034

Bontaș, M. G., Diacon, A., Călinescu, I., Necolau, M. I., Dinescu, A., Toader, G., Ginghină, R., Vizitiu, A.-M., Velicu, V., Palade, P., Istrate, M., & Rusen, E. (2022). Epoxy coatings containing modified graphene for electromagnetic shielding. *Polymers, 14*(12), Article 2508. https://doi.org/10.3390/polym14122508

Chen, K., Wang, P., Li, H., Cao, W., & Zheng, H. (2024). Enhanced microwave absorption in graphene-based composites: A study on the synergistic effect of ferrite integration and electromagnetic coupling. *Applied Surface Science, 669*, 160531. https://doi.org/10.1016/j.apsusc.2024.160531

Chen, Z., Xu, C., Ma, C., Ren, W., & Cheng, H. M. (2013). Lightweight and flexible graphene foam composites for high-performance electromagnetic interference shielding. *Advanced Materials, 25*(9), 1296–1300. https://doi.org/10.1002/adma.201204196

Dabla, M., Kaushik, S., Sharma, M., & Kuanr, B. K. (2025). Enhanced microwave absorption of Cr-substituted hard-soft Co-Ni ferrites conjugated with graphene oxide in the Ku band. *Ceramics International, 51*(29, Part C), 62057–62073. https://doi.org/10.1016/j.ceramint.2025.10.436

Dat, T. Q., Ha, N. T., & Hung, D. Q. (2017). Reduced graphene oxide-$Cu_{0.5}Ni_{0.5}Fe_2O_4$-polyaniline nanocomposite: Preparation, characterization and microwave absorption properties. *Journal of Electronic Materials, 46*(6), 3707–3713. https://doi.org/10.1007/s11664-017-5386-z

Dat, T. Q., Oanh, T. T., Thanh, N. K., Vi, L. D., Thin, P. V., Dieu, N. T. X., & Tran, N. (2025). Enhanced microwave absorption properties of $BaFe_{12}O_{19}/NiFe_2O_4$ composites prepared by hydrothermal method. *Ceramics International, 51*(25, Part A), 43543–43556. https://doi.org/10.1016/j.ceramint.2025.07.087

Dreyer, D. R., Park, S., Bielawski, C. W., & Ruoff, R. S. (2010). The chemistry of graphene oxide. *Chemical Society Reviews, 39*(1), 228–240. https://doi.org/10.1039/B917103G

Goldman, A. (2006). *Modern ferrite technology*. Springer. https://doi.org/10.1007/978-0-387-29413-1

Green, M., & Chen, X. (2019). Recent progress of nanomaterials for microwave absorption. *Journal of Materiomics, 5*, 503–541. https://doi.org/10.1016/j.jmat.2019.07.003

Gunasekaran, S., Thanrasu, K., Manikandan, A., Durka, M., Dinesh, A., Anand, S., Shankar, S., Slimani, Y., Almessiere, M. A., & Baykal, A. (2021). Structural, fabrication and enhanced electromagnetic wave absorption properties of reduced graphene oxide (rGO)/zirconium-substituted cobalt ferrite ($Co_{0.5}Zr_{0.5}Fe_2O_4$) nanocomposites. *Physica B: Condensed Matter, 605*, Article 412784. https://doi.org/10.1016/j.physb.2020.412784

Houbi, A., Aldashevich, Z. A., Atassi, Y., Telmanovna, Z. B., Saule, M., & Kubanych, K. (2021). Microwave absorbing properties of ferrites and their composites: A review. *Journal of Magnetism and Magnetic Materials, 529*, 167839. https://doi.org/10.1016/j.jmmm.2021.167839

Jiles, D. (2015). *Introduction to magnetism and magnetic materials* (3rd ed.). CRC Press. https://doi.org/10.1201/b18948

Krishnamoorthy, K., Veerapandian, M., Yun, K., & Kim, S. J. (2013). The chemical and structural analysis of graphene oxide with different degrees of oxidation. *Carbon, 53*, 38–49. https://doi.org/10.1016/j.carbon.2012.10.013

Luu, M. D., Luu, T. N., Le, T. H., Tran, Q. D., Pham, S. H., Nguyen, T. G., Nguyen, D. C., Doan, Q. T., & Nguyen, T. L. (2026). Defect-interface synergy in lightweight Fe_3O_4/rGO@SiO_2 nanocomposite for broadband electromagnetic wave absorption. *Materials Science and Engineering: B, 324*, Article 119023. https://doi.org/10.1016/j.mseb.2025.119023

Lv, H., Ji, G., Liang, X., Zhang, H., & Du, Y. (2015). A novel rod-like MnO_2@Fe loading on graphene giving excellent electromagnetic absorption properties. *Journal of Materials Chemistry C, 3*(19), 5056–5064. https://doi.org/10.1039/C5TC00525F

Marcano, D. C., Kosynkin, D. V., Berlin, J. M., Sinitskii, A., Sun, Z., Slesarev, A., Alemany, L. B., Lu, W., & Tour, J. M. (2010). Improved synthesis of graphene oxide. *ACS Nano, 4*(8), 4806–4814. https://doi.org/10.1021/nn1006368

Meng, F., Wang, H., Huang, F., Guo, Y., Wang, Z., Hui, D., & Zhou, Z. (2018). Graphene-based microwave absorbing composites: A review and prospective. *Composites Part B: Engineering, 137*, 260–277. https://doi.org/10.1016/j.compositesb.2017.11.023

Naito, Y., & Suetake, K. (1971). Application of ferrite to electromagnetic wave absorber and its characteristics. *IEEE Transactions on Microwave Theory and Techniques, 19*(1), 65–72. https://doi.org/10.1109/TMTT.1971.1127446

Nguyen, V. Q., Luu, M. D., Pham, D. T., To, T. L., Tran, Q. D., Pham, S. H., Hoang, A. S., Doan, Q. T., & Nguyen, T. L. (2024). Facile process for cost-effective layer-by-layer rGO/SiO_2 structure for high microwave absorption. *Ceramics International, 50*(22), 47136–47144. https://doi.org/10.1016/j.ceramint.2024.09.065

Shu, R., Zhang, G., Zhang, J., Wang, X., Wang, M., Gan, Y., Shi, J., & He, J. (2018). Synthesis and high-performance microwave absorption of reduced graphene oxide/zinc ferrite hybrid nanocomposite. *Materials Letters, 215*, 229–232. https://doi.org/10.1016/j.matlet.2017.12.108

Singh, S. K., Penke, Y. K., Ramkumar, J., Akhtar, M. J., & Kar, K. K. (2022). Facile synthesis of Al-substituted Cu-ferrite infused reduced graphene oxide (rGO) nanohybrid for improving microwave absorption at gigahertz frequencies. *Journal of Alloys and Compounds, 901*, Article 163659. https://doi.org/10.1016/j.jallcom.2022.163659

Sugimoto, S. (2011). Current status and recent topics of rare-earth permanent magnets. *Journal of Physics D: Applied Physics, 44*, 064001. https://doi.org/10.1088/0022-3727/44/6/064001

Tho, P. T., Tran, N., Xuan, C. T. A., Dat, T. Q., Bach, T. N., Ho, T. A., Tuan, N. Q., Khan, D. T., Tuyen, N. L., & Khien, N. V. (2024). Microwave absorption performance of $La_{1.5}Sr_{0.5}NiO_4$/$SrFe_{12}O_{19}$ composites with thin matching thickness. *Ceramics International, 50*(22, Part B), 46683–46694. https://doi.org/10.1016/j.ceramint.2024.09.020

Tran, Q. D., Le, D. V., Nguyen, T. H., Nguyen, N. L., To, T. L., Vu, D. L., & Tran, N. (2026). Tunable microwave absorption of bio-carbon/$CuFe_2O_4$: A trade-off for broadband versus stealth performance. *Ceramics International, 52*, 4464–4476. https://doi.org/10.1016/j.ceramint.2025.12.220

Tran, T. V. N., Nguyen, T. L., To, T. L., & Tran, Q. D. (2024). Enhancement of the microwave absorption properties of the $SrFe_{12}O_{19}$@Fe_3O_4@rGO composite material. *Journal of Science: Advanced Materials and Devices, 9*(3), Article 100758. https://doi.org/10.1016/j.jsamd.2024.100758

Zheng, Y., Ma, Z., Weng, X., Cheng, L., & Li, Z. (2025). Preparation and enhanced microwave absorption properties of Mg-Co ferrite/microcrystalline graphene oxide composites. *Journal of Alloys and Compounds, 1037*, Article 182603. https://doi.org/10.1016/j.jallcom.2025.182603